Near-Infrared Polarimetric Image Sensors Based on Ordered Sulfur-Passivation GaSb Nanowires Arrays

Kai Zhang,‡[1,3] Zhihui Ren,‡[2,5] Huichen Cao,[1] Lingling Li,[2] Ying Wang,[1] Wei Zhang,[1] Yubao Li,[1] Haitao Yang,[2] You Meng,[4] Johnny C. Ho,*[4] Zhongming Wei*[2] and Guozhen Shen*[2,6]*

[1]Hebei Key Lab of Optic-electronic Information and Materials, the College of Physics Science and Technology, Hebei University, Baoding 071002, China

[2]State Key Laboratory of Superlattices and Microstructures, Institute of Semiconductors, Chinese Academy of Sciences, Beijing 100083, China

[3]Institute of Physics, Chinese Academy of Sciences and University of Chinese Academy of Sciences, Beijing 100190, China

[4]Department of Materials Science and Engineering, and State Key Laboratory of Terahertz and Millimeter Waves, City University of Hong Kong, Hong Kong 999077, China

[5]Centre for Quantum Physics, Key Laboratory of Advanced Optoelectronic Quantum Architecture and Measurement (MOE), School of Physics, Beijing Institute of Technology, Beijing 100081, China.

[6] School of Integrated Circuits and Electronics, Beijing Institute of Technology, Beijing 100081, China

* Address Correspondence to Y. L. (liyubao@hbu.edu.cn), J. H. (johnnyho@cityu.edu.hk), Z. W. (zmwei@semi.ac.cn) and G. S. (gzshen@semi.ac.cn)

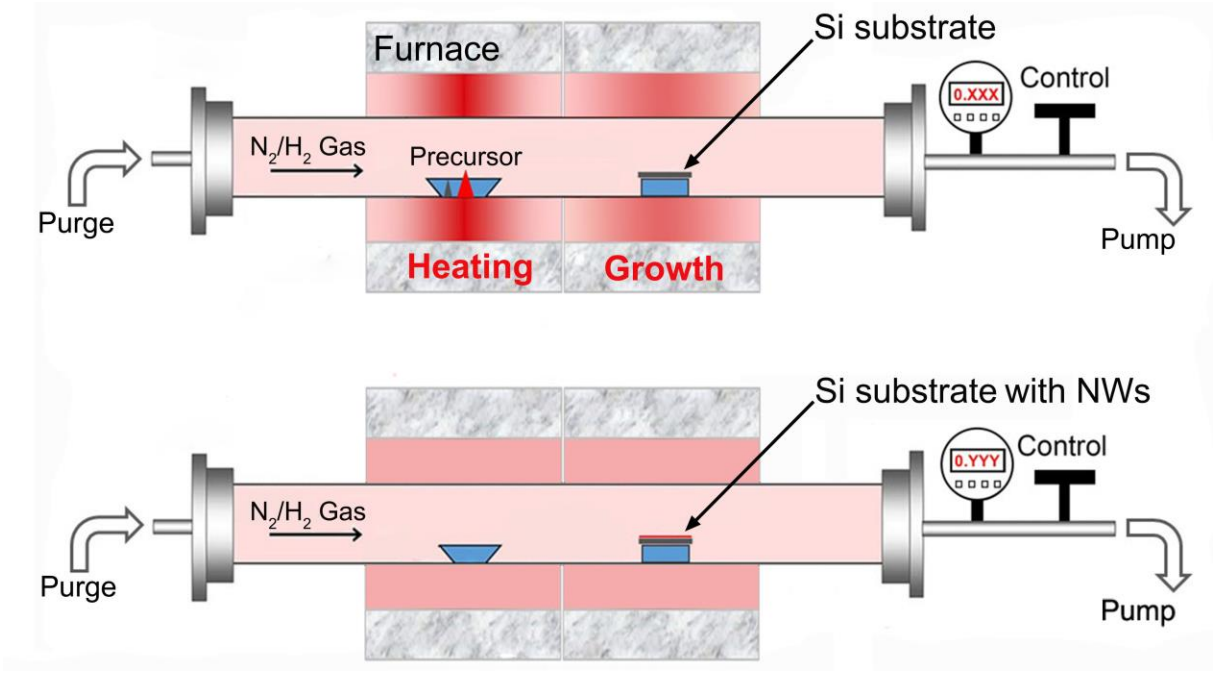

Figure S1. Schematic illustration of the CVD process to synthesize sulfur-passivation GaSb (S-GaSb) NWs.

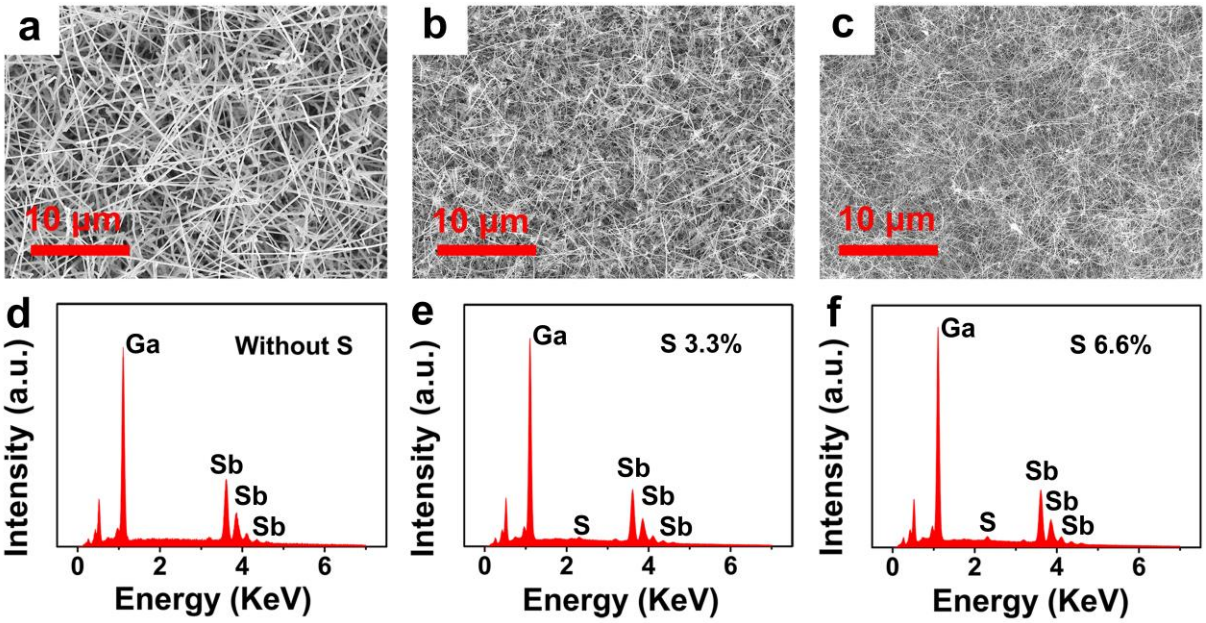

Figure S2. SEM images of large areas of as-grown S-GaSb NWs. (a) pure GaSb NWs, (b) S-GaSb NWs with S 3.3 mass percent in the precursor, (c) S-GaSb NWs with S 6.6 mass percent in the precursor. (d-f) EDS images corresponding to SEM images a-c.

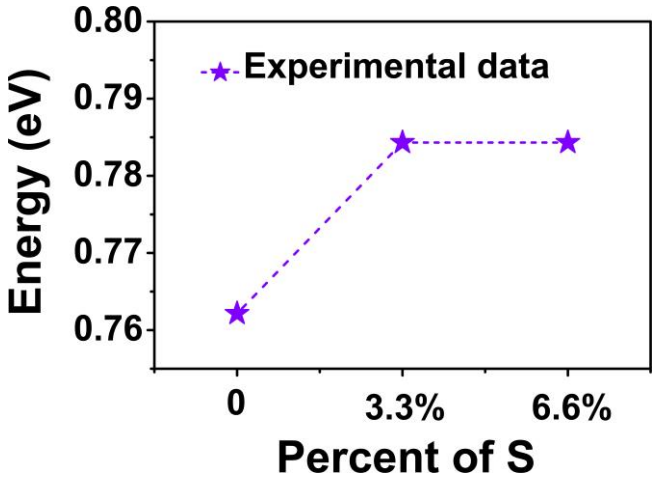

Figure S3. Corresponding energy of PL spectra peak of pure GaSb NWs, S-GaSb NWs with S 3.3% and S-GaSb NWs with S 6.6%.

The PL spectra was measured using an iHR320 infrared spectrometer. The experiment condition of vacuum and 77 K low temperature was realized in a cold trap. The excitation light was 800 nm (pulse width 20 ps, repetition frequency 80 MHz) generated by a monochromatic laser. The power intensity of the excitation light was fixed at 2 mW making sure that the light power intensity on each sample was kept a constant value.

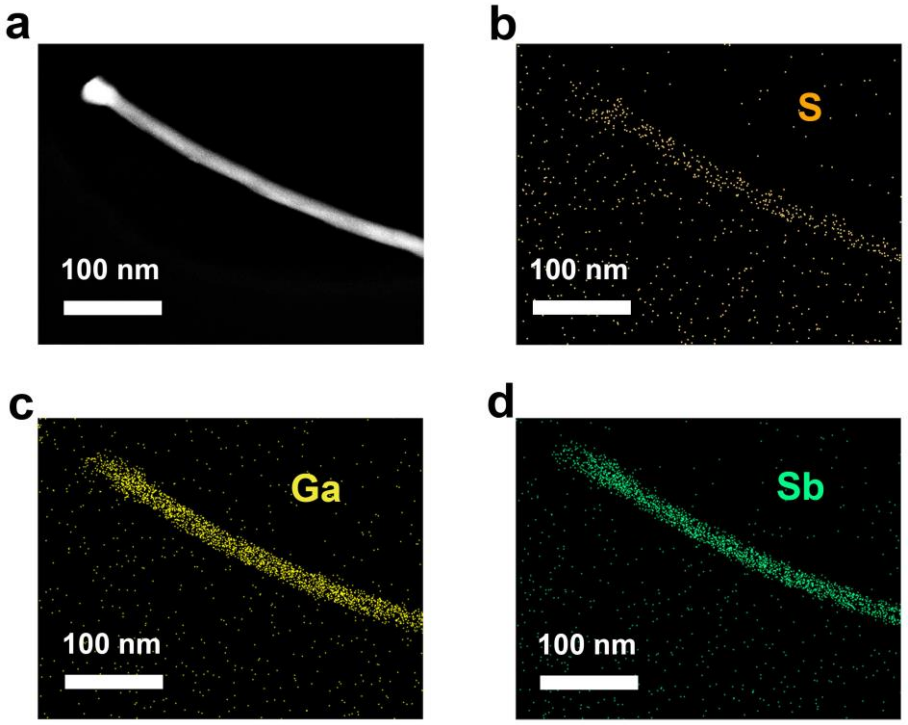

Figure S4. (a) STEM image of single S-GaSb NW with S 6.6%. Corresponding EDS element mapping of (b) S, (c) Ga, and (d) Sb.

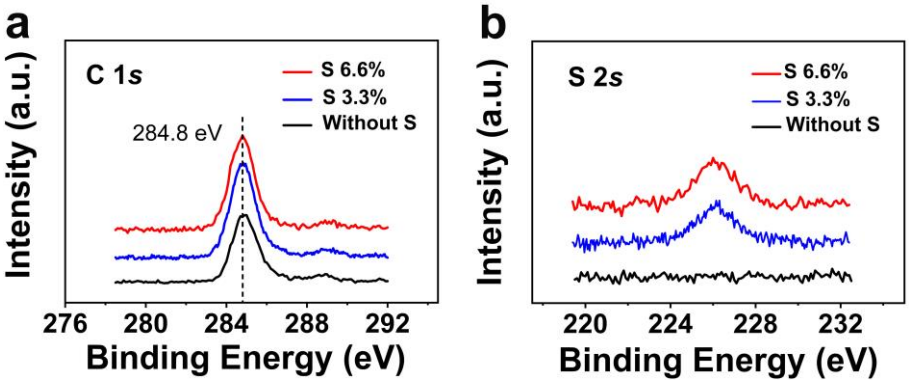

Figure S5. XPS spectra of as-grown S-GaSb NWs. (a) C 1*s* peaks calibrated as 284.8 eV, (b) S 2*s* peaks.

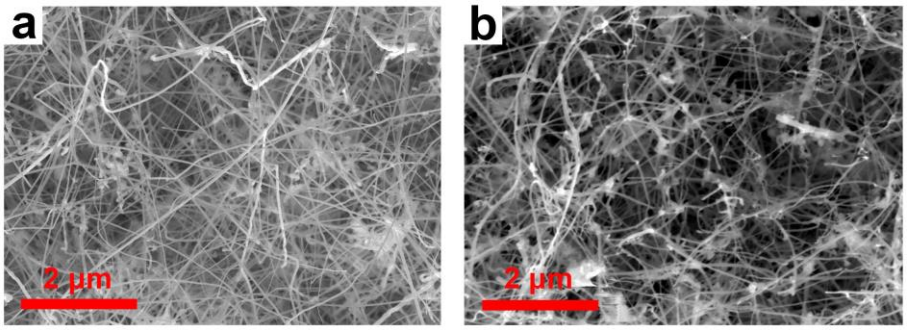

Figure S6. The SEM images of the S-GaSb NWs with S 6.6% (a) before etching, (b) after etching 40 s with Ar ions.

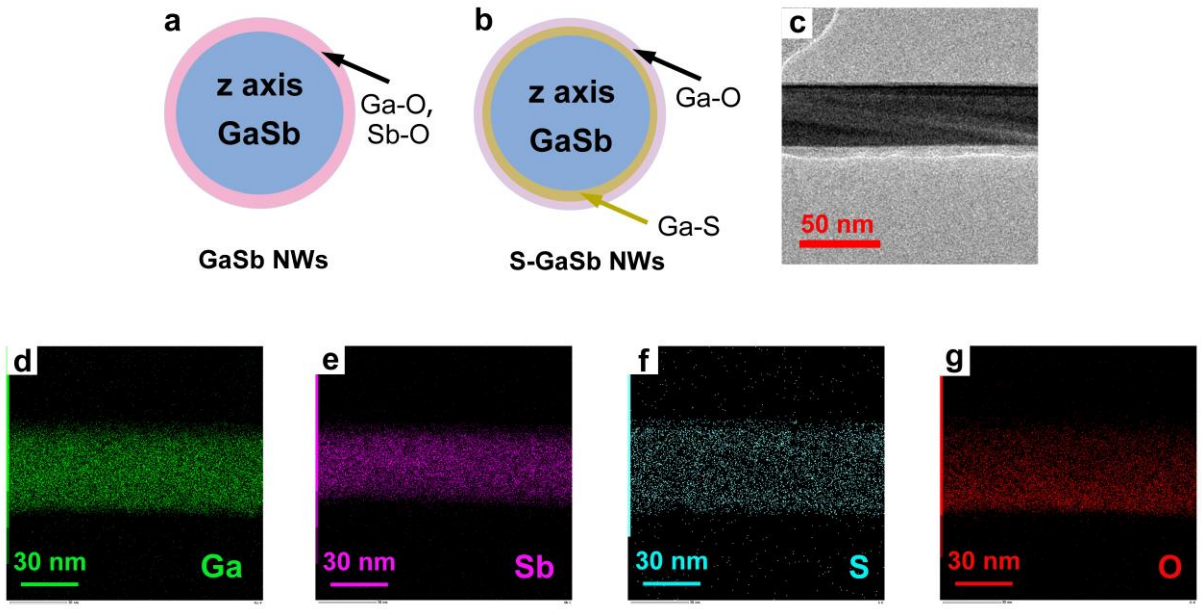

Figure S7. Schematic illustration of the surface structure of (a) GaSb NW, (b) S-GaSb NW. (c) STEM image of S-GaSb NWs with S 50%. (d-g) Corresponding EDS element mapping of Ga, Sb, S, O.

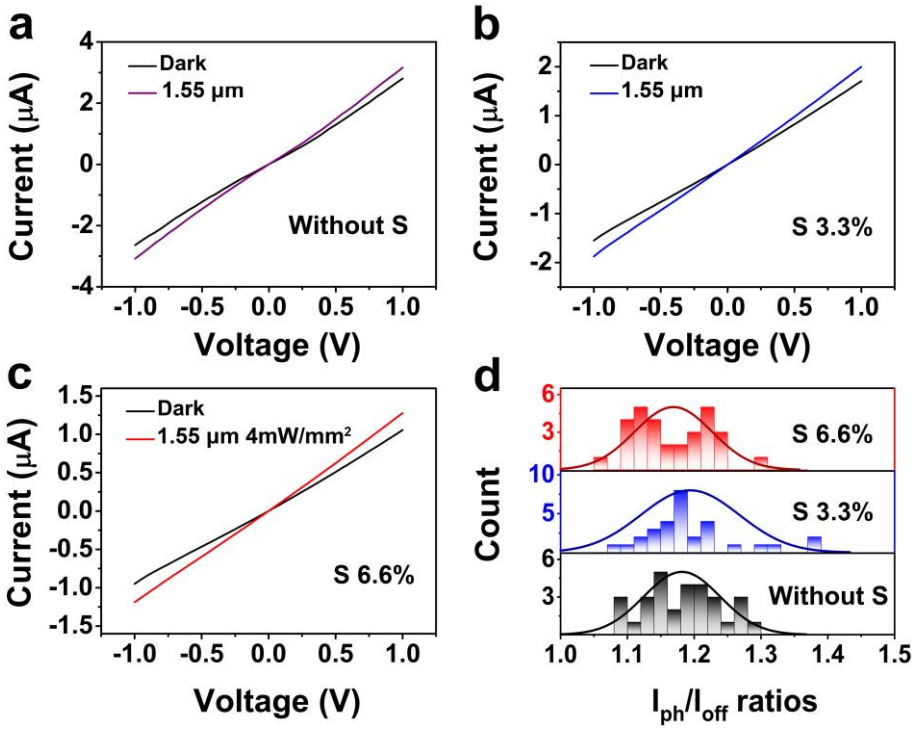

Figure S8. Typical *I-V* curves of photodetectors based on (a) pure GaSb NW, (b) S-GaSb NW with S 3.3%, (c) S-GaSb NW with S 6.6%. (d) The statistical results of I_{ph}/I_{off} ratios of 30 NW-devices of pure GaSb NWs, S-GaSb NWs with S 3.3%, and S-GaSb NWs with S 6.6%, respectively. The measurement condition is under the incident 1.55 μm light with 4 mw/mm^2 at 1 V bias.

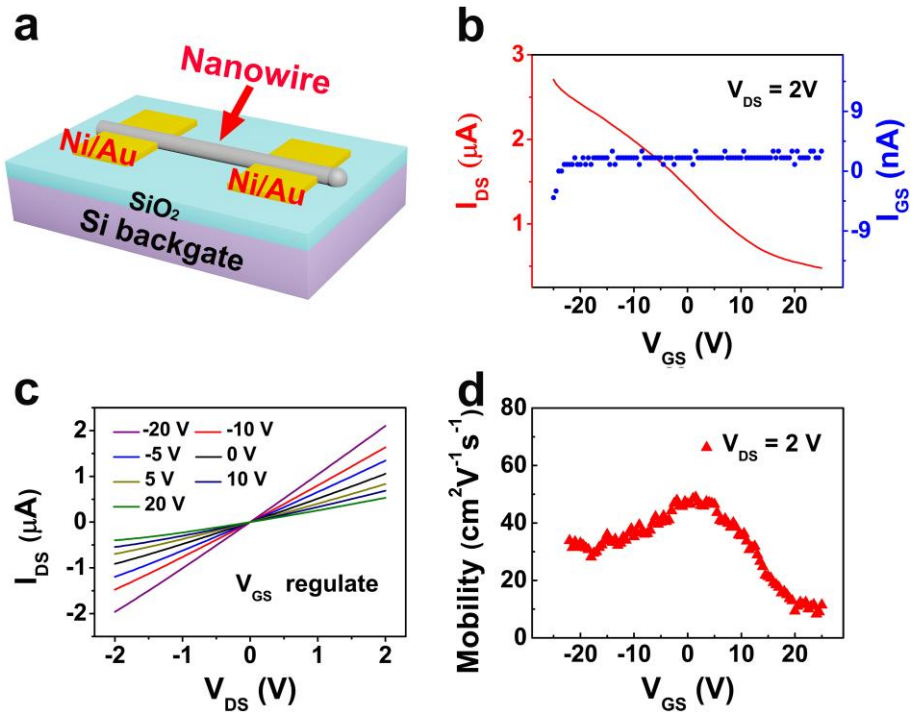

Figure S9 The FET properties of the S-GaSb NW-based device. (a) Schematic illustration of the FET structure based on the S-GaSb NW. (b) Transfer characteristic. (c) Output characteristics. (d) FET hole mobility.

The Field-Effect Transistors (FET) properties based on the S-GaSb NW are displayed in Figure S9. Figure S9a is the schematic illustration of the back-gate structure of the FET device where the monocrystalline (100) Si and the SiO_2 (300 nm) dielectric layer are back gate. Figure S9b displays the relationship between I_{DS} and I_{GS} *versus* V_{GS} at a given V_{ds} = 2 V. The value of I_{DS} is 3 orders of magnitude higher than that of I_{GS}, certifying perfectly electric transport properties of the as-fabricated FET device. The typical p-type transfer behavior is observed, where I_{DS} decreases obviously with the increasement of V_{GS}, affirming the p-type semiconductor of as-grown S-GaSb NWs. In Figure 2e, the device also reveals good output characteristics. The field-effect hole mobility μ_h of the S-GaSb NW-based FET could be acquired by the following equations:[1-4]

$$C_i \approx \frac{2\pi\varepsilon_o\varepsilon_r L}{\mathrm{In}(2h/r)} \quad (1)$$

$$\mu_h = \frac{g_m L^2}{(V_{DS} C_i)} \quad (2)$$

where g_m is the transconductance defined as $(dI_{DS})/(dV_{GS})|V_{DS}$, C_i is the back gate capacitance, ε_o is the vacuum dielectric constant (ε_o = 8.85×10^{-12} F/m), ε_r is the relative dielectric constant of SiO_2 (ε_r = 3.9), L is the S-GaSb NW length in the channel (10 μm), h is the thickness of SiO_2 dielectric layer (300 nm), and r is the radius of the NW (24 nm). The calculated value of μ_h is demonstrated in Figure 2c and the peak value is 48.9 cm^2 V^{-1} s^{-1}.

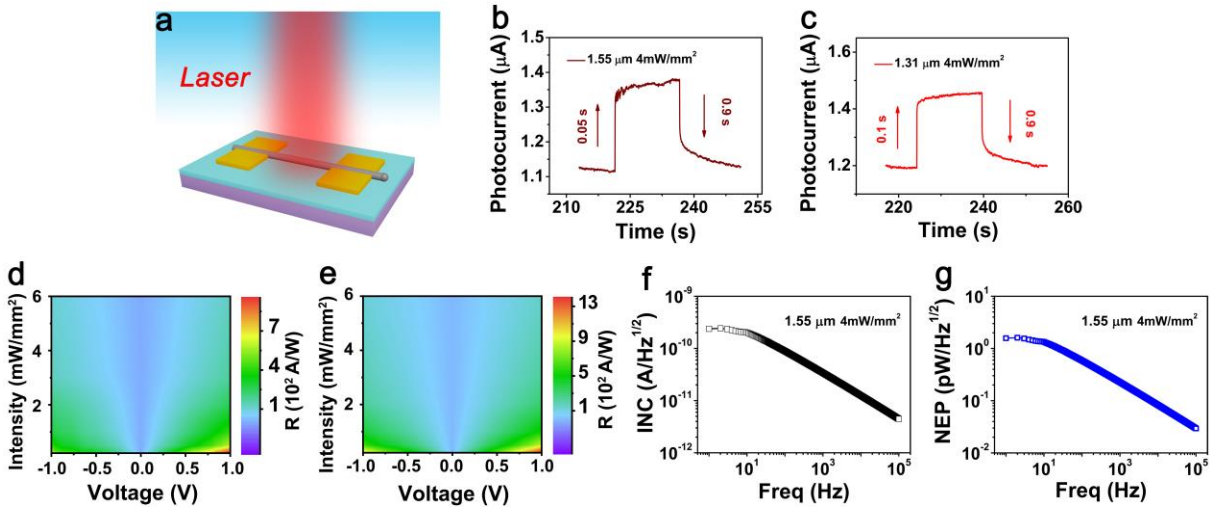

Figure S10 The near-infrared photoresponse performances of the S-GaSb NW-based photodetector. (a) Schematic illustration of the photodetector under the illumination of near-infrared light. (b) Response time of the photodetector for 1.55 μm light and (c) for 1.31 μm light. (d) 2D map of the R_λ as a function of bias voltage and 1.55 μm light power intensity. (e) 2D map of the R_λ as a function of bias voltage and 1.31 μm light power intensity. (f) The measured *INC* curves of the photodetector and (f) the calculated value of noise equivalent power (*NEP*) corresponding to the value of *INC*.

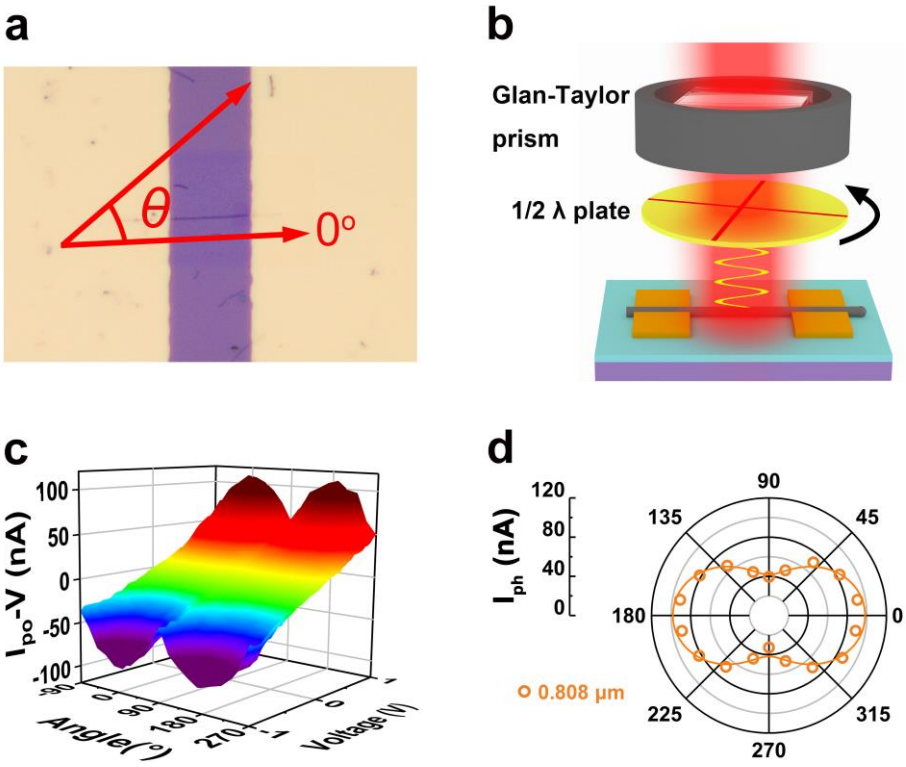

Figure S11 Polarized photoresponses of the S-GaSb NW-based photodetector. (a) Photograph of the device corresponding to the SEM image of Figure 3a. (b) Schematic illustration of the device under the illumination of linear polarization light. (c) 3D surface maps of polarized photocurrent I_{po} (z-axis) *versus* V_d (x-axis) and polarized angle (y-axis) for incident linear polarization light of 0.808 μm. (d) Evolution of the I_{po} with the polarized angle of 0.808 μm light at 1 V bias.

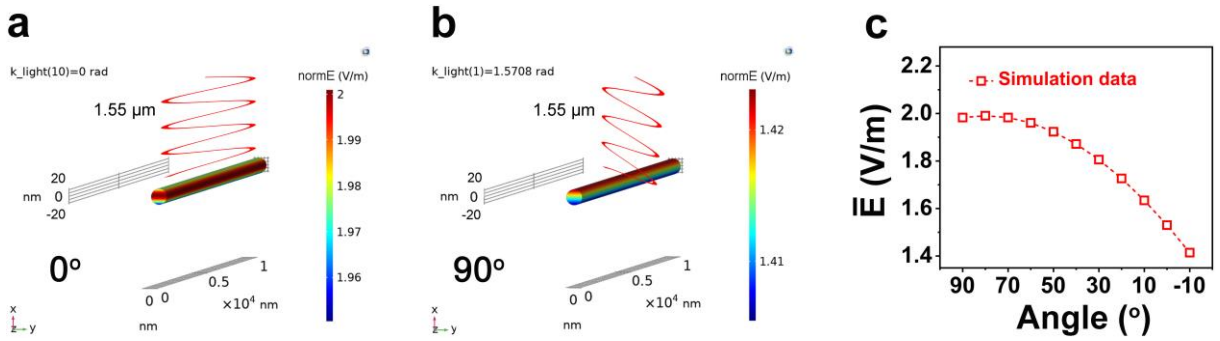

Figure S12 COMSOL simulation of light electric field *E* inside the S-GaSb NW under 1.55 μm linear polarization light. (a) *E* distribution inside NW under light polarization angle parallel to NW long-axis. (b) *E* distribution inside NW under light with polarized angle perpendicular to NW long-axis. (c) Calculated average of the *E* intensity inside the NW under 1.55 μm linear polarization light with different direction from -10° to 90°.

The numerical simulation was performed using a commercial software COMSOL Multiphysics 5.4. According to the SEM image of the S-GaSb NW in Figure 3a, a cylinder of GaSb NW with 48 nm diameter, 10 μm length was built in the vacuum as shown in Figure S12a-b. Two problems are needed to point out. The first one, compared with the 48 nm diameter of entire NW the 3 nm surface S-passivation layer could be ignored. The second one, the polarized properties of the S-GaSb NW-based photodetector is measured in open atmosphere at room temperature. However, due to the dielectric constant of air almost equal to that of vacuum, the model of GaSb NW cylinder could be built in the vacuum.[5, 6] The linear polarization light of 1.55 μm was employed as external exciting source which illuminated the NW from the top. The light power received on the NW surface was 10 nW equivalent to 1.33 mW/mm^2. In order to simulate the real experiment conditions, a bias of 1 V was also added between the NW two side. The background electric field was 1 V/m. The distribution of light electric field *E* inside the NW was calculated under above linear polarization 1.55 μm light with various direction angles from -10° to 90°.

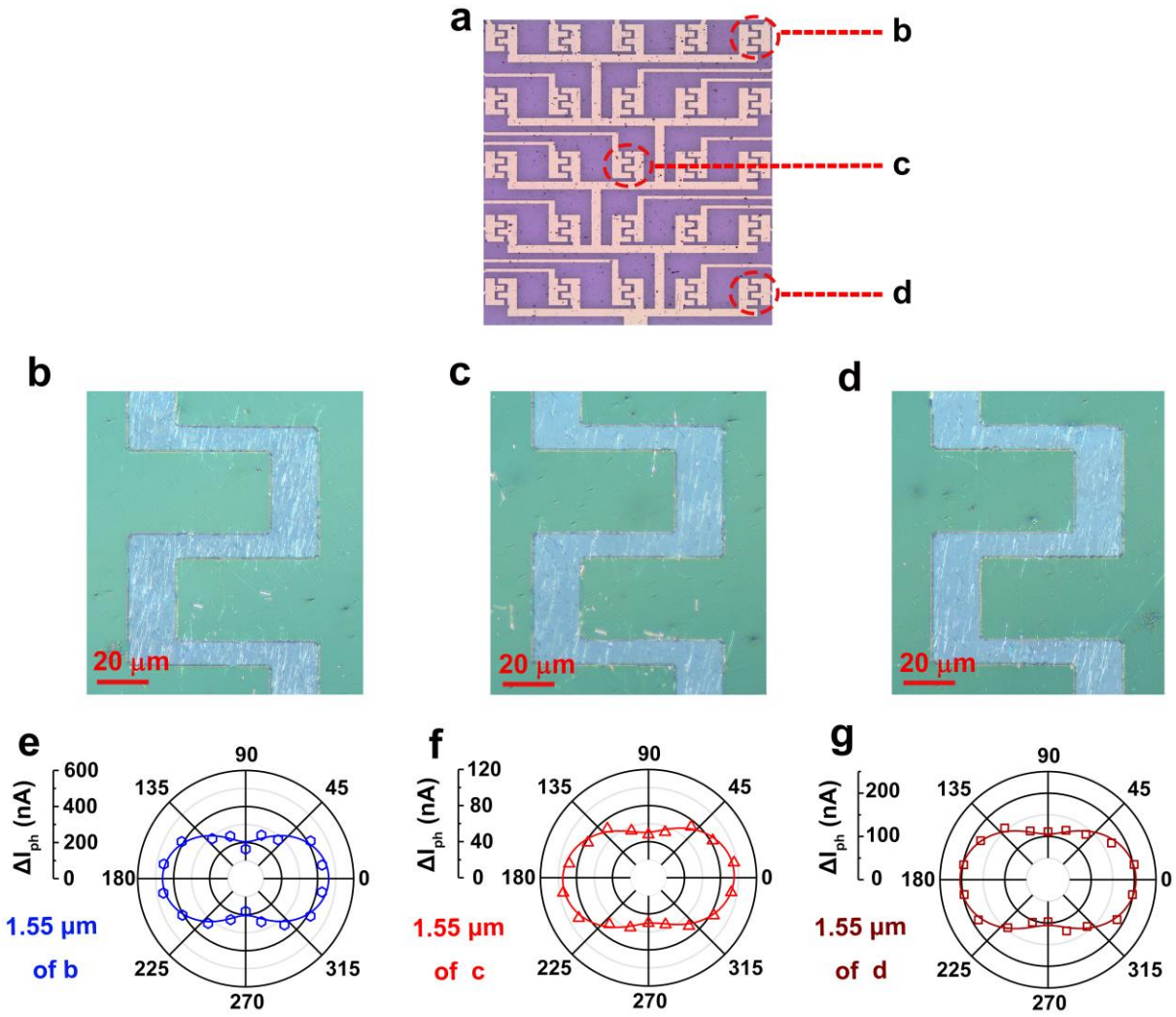

Figure S13 (a) Photograph of the 5 × 5 pixels flexible polarimetric image sensor based on ordered S-GaSb NWs arrays. (b-d) High-magnification photographs corresponding to the pixels in a. (e-f) Polarized photoresponse properties of corresponding pixel in b-d.

Noticeably, the photograph of Figure 5f and Figure S13a was taken from the flexible polarimetric image sensor placed on a SiO_2 chip, because the PET substrate is transparent and poor-reflectivity.

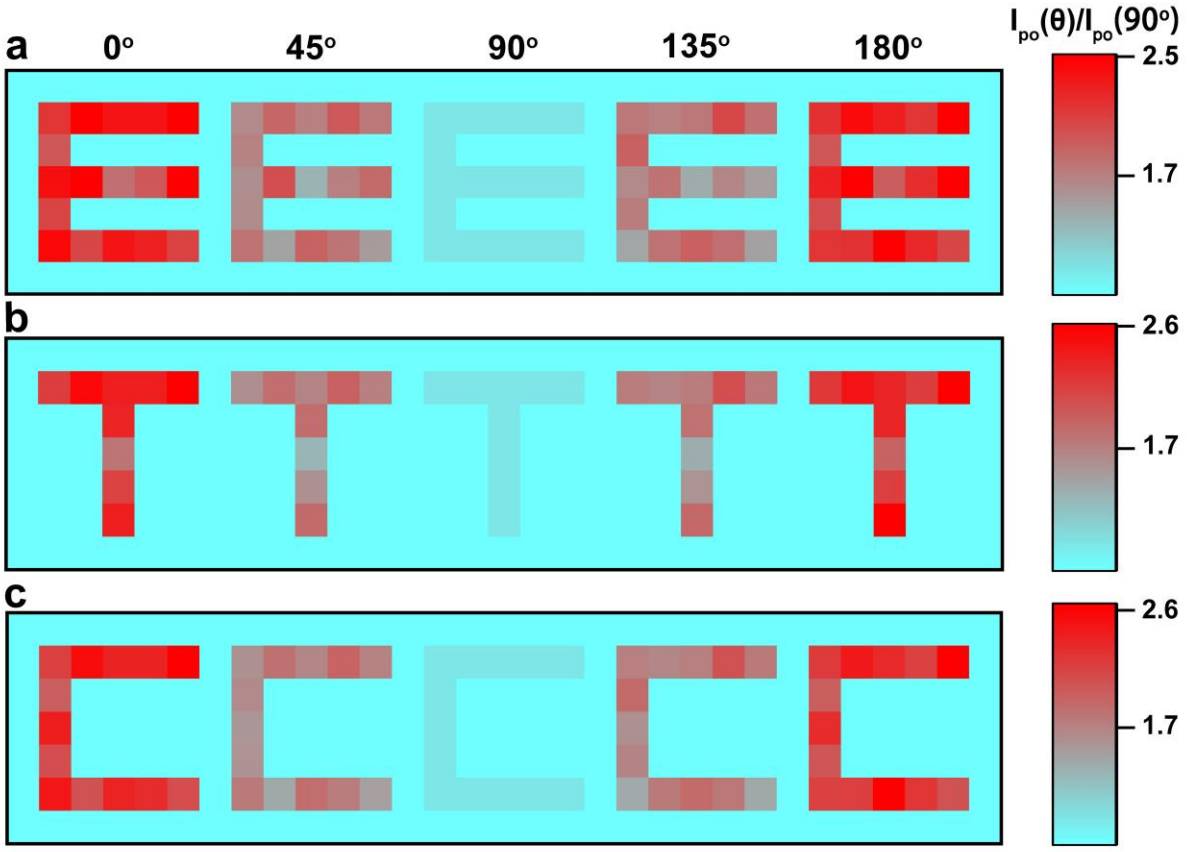

Figure S14 The output 2D images of the polarimetric image sensor corresponding to (a) "E" mask, (b) "T" mask and (c) "C" mask. All the polarized signals are normalized by $I_{po}(\theta)/I_{po}(90^{o})$.

Table S1 The summary of the responsivity (R_λ) and the detectivity (D*) of the S-GaSb NW-based photodetector (Figure 3a) for 1.55 μm incident light.

Wavelength	Bias voltage	Power intensity (mW/mm^2)	R_λ (AW^{-1})	D* (Jones)
1.55 μm	1 V	0.25	939.24	1.10×10^{11}
		0.5	588.83	6.87×10^{10}
		1	414.96	4.84×10^{10}
		2	247.12	2.88×10^{10}
		3	167.81	1.96×10^{10}
		4	147.93	1.73×10^{10}
		5	135.51	1.58×10^{10}
		6	119.87	1.40×10^{10}

Table S2 The summary of the responsivity (R_λ) and the detectivity (D*) of the S-GaSb NW-based photodetector (Figure 3a) for 1.31 μm incident light

wavelength	Bias voltage	Power intensity (mW/mm^2)	R_λ (AW^{-1})	D* (Jones)
1.31 μm	1 V	0.25	1375.98	1.61×10^{11}
		0.5	857.41	1.01×10^{11}
		1	513.16	6.02×10^{10}
		2	303.72	3.56×10^{10}
		3	225.37	2.64×10^{10}
		4	194.14	2.28×10^{10}
		5	165.75	1.94×10^{10}
		6	146.48	1.72×10^{10}

Table S3 The summary of typical researches of the ordered NWs arrays in recent reports.

Material	Assembled structure	Application	Reference
Ag NWs	Ordered NWs arrays	Transparent conductive electrodes	[7]
P(SP-alt-C10)	Nanofiber Composites	Strain sensors	[8]
$CsPbBr_3$ NWs	Ordered arrays	Polarized photoluminescence	[9]
Si NWs	Ordered arrays	MOSFET devices	[10]
GaSb NWs	Ordered arrays	Photodetectors	[11]
CNTs	Ordered arrays	Logic circuits	[12]
GaSb NWs	Ordered arrays	Near-infrared polarimetric image sensors	This work

Table S4 The dichroic ratio comparison between single S-GaSb NW, ordered S-GaSb NWs arrays polarization photodetectors in this work and other 1D or quasi-1D polarization photodetectors in previous reports.

Material	Structure	Origin of polarization	Response wavelength (nm)	Dichroic ratio	Reference
KNb_3O_8	Nanobelt	Low-symmetry crystal structure	254	1.62	[13]
SbI_3	Nanowire		450	1.16	[14]
ZrS_3	Nanoribbon		450	2.55	[15]
$Sn^{II}Sn^{IV}S_3$	Quasi-nanowire		532	1.3	[16]
Sb_2Se_3	Nanowire		532	1.63	[17]
$Nb_{1-x}Ti_xS_3$	Nanowire		633	1.75	[18]
Sb_2S_3	Nanowire		808	1.84	[19]
S-GaSb	Nanowire	Anisotropic 1D geometry structure	1550	2.65	This work
	Ordered nanowire arrays		1550	2.04	

(1) Chen, G.; Liang, B.; Liu, X.; Liu,Z.; Yu, G.; Xie, X. M.; Luo, T.; Chen, D.; Zhu, M. Q.; Shen, G. Z.; Fan, Z. High-Performance Hybrid Phenyl-C61-Butyric Acid Methyl Ester/Cd_3P_2 Nanowire Ultraviolet-Visible-Near Infrared Photodetectors. *ACS Nano* **2014**, *8*, 787-796.

(2) Yu, G.; Liang, B.; Huang, H.; Chen, G.; Liu, Z.; Chen, D.; Shen, G. Contact printing of horizontally-aligned p-type Zn_3P_2 nanowire arrays for rigid and flexible photodetectors. *Nanotechnology* **2013**, *24*, 095703.

(3) Cui, Y.; Duan X. F.; Hu, J. T.; Lieber, C. M. Doping and Electrical Transport in Silicon Nanowires. *J. Phys. Chem. B* **2000**, *104*, 5213-5216.

(4) Zhang, K.; Chai, R.; Shi, R.; Lou, Z.; Shen, G., Self-catalyzed growth of GaSb nanowires for high performance ultraviolet-visible-near infrared photodetectors. *Sci. China Mater.* **2019**, *63*, 383-391.

(5) Wang, J. F.; Gudiksen, M. S.; Duan, X. F.; Cui, Y.; Lieber, C. M. Highly Polarized Photoluminescence and Photodetection from Single Indium Phosphide Nanowires. *Science* **2001**, *293*, 1455-1457.

(6) Liu, Z.; Chen, G.; Liang, B.; Yu, G.; Huang, H. T.; Chen, D.; Shen, G. Z. Fabrication of high-quality ZnTe nanowires toward high-performance rigid/flexible visible light photodetectors. *Opt. Express* **2013**, *21*, 7799-7810.

(7) Cho, S.; Kang, S.; Pandya, A.; Shanker, R.; Khan, R.; Lee, Y.; Park, J.; Stephen L. Craig, S. L.; Ko, H. Large-Area Cross-Aligned Silver Nanowire Electrodes for Flexible, Transparent, and Force-Sensitive Mechanochromic Touch Screens. *ACS Nano* **2017**, *11*, 4346-4357.

(8) Raisch, M.; Genovese, D.; Zaccheroni, N.; Schmidt, S. B.; Focarete, M. L.; Sommer, M.;Gualandi C. Highly Sensitive, Anisotropic, and Reversible Stress/Strain-Sensors from Mechanochromic Nanofiber Composites. *Adv. Mater*. **2018**, *30*, 1802813.

(9) Zhou, N.; Bekenstein Y.; Eisler C. N.; Zhang, D.; Schwartzberg, A. M.; Yang, P. D.; Alivisatos, A. P.; Lewis, J. A. Perovskite nanowire-block copolymer composites with digitally programmable polarization anisotropy. *Sci*. *Adv*. **2019**, *5*, eaav8141.

(10) Yao, J.; Yan, H.; Lieber, C. M. A nanoscale combing technique for the large-scale assembly of highly aligned nanowires. *Nat*. *Nanotech*. **2008**, *3*, 88-92.

(11) Liu, D.; Liu, F.; Liu, Y.; Pang, Z. Y.; Zhuang, X.; Yin, Y. X.; Dong, S.; He, L.; Tan, Y.; Liao, L.; Chen, F.; Yang, Z. X. Schottky-Contacted High-Performance GaSb Nanowires Photodetectors

Enabled by Lead-Free All-Inorganic Perovskites Decoration. *Small* **2022**, DOI: 10.1002/smll.202200415.

(12) Liu, L. J.; Han, J.; Xu, L.; Zhou, J. S.; Zhao, C. Y.; Ding, S. J.; Shi, H. W.; Xiao, M. M.; Ding, L.; Ma, Z.; Jin, C. H.; Zhang, Z. Y.; Peng, L. M. Aligned, high-density semiconducting carbon nanotube arrays for high-performance electronics. *Science* **2020**, *368*, 850-856.

(13) Ping, Y.; Long, H.; Liu, H.; Chen, C.; Zhang, N.; Jing, H.; Lu, J.; Zhao, Y.; Yang, Z.; Li, W.; Ma, F.; Fang, X.; Wei, Z. M.; Xu, H. Polarization Sensitive Solar-Blind Ultraviolet Photodetectors Based on Ultrawide Bandgap KNb_3O_8 Nanobelt with Fringe-Like Atomic Lattice. *Adv. Funct. Mater.* **2022**, online, 2111673.

(14) Xiao, M.; Yang, H.; Shen, W.; Hu, C.; Zhao, K.; Gao, Q.; Pan, L.; Liu, L.; Wang, C.; Shen, G. Z.; Deng, H. X.; Wen, H.; Wei, Z. M. Symmetry-Reduction Enhanced Polarization-Sensitive Photodetection in Core-Shell SbI_3/Sb_2O_3 van der Waals Heterostructure. *Small* **2020**, *16*, e1907172.

(15) Wang, X. T.; Wu, K. D.; Blei, M.; Wang, Y.; Pan, L. F.; Zhao, K.; Shan, C. X.; Lei, M.; Cui, Y.; Chen, B.; Wright, D.; Hu, W. D.; Tongay, S.; Wei, Z. M. Highly Polarized Photoelectrical Response in vdW ZrS_3 Nanoribbons. *Adv. Electron.Mater.* **2019**, *5*, 1900419.

(16) Yang, H. P., L. F.; Wang, X. T.; Deng, H. X.; Zhong, M. Z.; Zhou, Z. Q.; Lou, Z.; Shen, G. Z.; Wei, Z. M. Mixed-Valence-Driven Quasi-1D $Sn^{II}Sn^{IV}S_3$ with Highly Polarization-Sensitive UV-vis-NIR Photoresponse. *Adv. Funct. Mater.* **2019**, *29*, 1904416.

(17) Ma, Z.; Chai, S.; Feng, Q.; Li, L.; Li, X.; Huang, L.; Liu, D.; Sun, J.; Jiang, R.; Zhai, T.; Xu H., Chemical Vapor Deposition Growth of High Crystallinity Sb_2Se_3 Nanowire with Strong Anisotropy for Near-Infrared Photodetectors. *Small* **2019**, *15*, e1805307.

(18) Yang, S.; Wu, M.; Shen, W.; Huang, L.; Tongay, S.; Wu, K.; Wei, B.; Qin, Y.; Wang, Z.; Jiang, C.; Hu, C. Highly Sensitive Polarization Photodetection Using a Pseudo-One-Dimensional $Nb_{(1-x)}Ti_xS_3$ Alloy. *ACS Appl. Mater. Interfaces* **2019**, *11*, 3342-3350.

(19) Zhao, K.; Yang, J.; Zhong, M.; Gao, Q.; Wang, Y.; Wang, X.; Shen, W.; Hu, C.; Wang, K.; Shen, G. Z.; Li, M.; Wang, J.; Hu, W. D.; Wei, Z. M. Direct Polarimetric Image Sensor and Wide Spectral Response Based on Quasi-1D Sb_2S_3 Nanowire. *Adv. Funct. Mater.* **2020**, *31*, 2006601.